Surface bonding:
From molecules to microparticles

Jukka Katainen

Laboratory of Physics
Helsinki University of Technology
Espoo, Finland

Dissertation for the degree of Doctor of Science in Technology to be presented with due permission of the Department of Engineering Physics and Mathematics for public examination and debate in Auditorium K at Helsinki University of Technology (Espoo, Finland) on the 9th of January, 2007, at 13 o'clock.

Dissertations of Laboratory of Physics, Helsinki University of Technology
ISSN 1455-1802

Dissertation 143 (2007):
Jukka Katainen: Surface bonding: From molecules to microparticles
ISBN-13 978-951-22-8568-6 (print)
ISBN-10 951-22-8568-1 (print)
ISBN-13 978-951-22-8569-3 (electronic)
ISBN-10 951-22-8569-X (electronic)

Otamedia OY
ESPOO 2007

Abstract

Surfaces play an active role in many applications ranging from molecular level to macroscopic phenomena. On a molecular level, surface bonds are utilized *e.g.* in catalysis, sensor applications and coating technology. Bonds in the molecular level are usually formed between single atoms with very limited interaction range originating from the charge transfer between the species. On the macroscopic side, surfaces or interfaces between bulk objects have interaction even when the surfaces are inert in the chemical sense. The attractive interaction is caused by long range electrostatic forces acting on the whole interface. However, the interactions between bulk objects are usually localized in the range of hundreds of nanometers or some micrometers due to the surface roughness present on all practical surfaces. This interaction is exploited *e.g.* in pharmaceutical industry but it has also disadvantages *e.g.* in energy production, where ash particles contaminate heat exchanger surfaces.

This work consist of two parts including studies with a well defined surface in ultra high vacuum and studies with practical surfaces in ambient conditions.

Low energy electron diffraction (LEED) has been utilized in determination of the adsorption structures of benzene on Co(0001) surface. The adsorption geometry has been studied using tensor LEED and Density Functional Theory calculations. The studies revealed two adsorption structures in different temperatures. The saturation coverage is 0.143 monolayers and the benzene ring lays flat on an hcp site. The carbon–hydrogen bonds of the benzene ring are slightly bend away from the substrate.

Adhesion of small oxide particles to oxide surfaces has been studied using scanning force microscope. The surface geometry was observed to play very important role in the adhesion. Particularly, the relative lengthscale of the particles and surface features has an important effect. A new model for estimating adhesion on rough surfaces has been developed. By tuning the surface features, the strength of adhesion may significantly be changed. Adhesion in humid conditions has been studied experimentally as well as with numerical simulations. In humid conditions, when the surfaces are hydrophilic, a capillary bridge forms between the particle and the surface increasing the adhesion. The bridge changes the nature of adhesion from van der Waals type to surface tension induced adhesion. The shape and size of the particle and the geometry of the surface all contribute to the adhesion behavior in humid conditions.

Tiivistelmä

Pinnoilla on merkittävä vaikutus moniin sovelluksiin molekyylitasolta aina makroskooppisiin ilmiöihin saakka. Molekyylitason sitoutumista pintoihin käytetään hyväksi mm. katalyyttisissä prosesseissa, antureissa ja pinnoitustekniikoissa. Yksittäisten molekyylien ja pinnan väliset sidokset aiheutuvat varausten vaihdosta molekyylin ja pinnan atomien välillä, mistä johtuen sidokset ovat hyvin paikallisia. Myös kiinteiden, makroskooppista kokoluokkaa olevien kappaleiden välillä esiintyy vuorovaikutusta, vaikka ne olisivatkin sähköisesti neutraaleja ja kemiallisesti inerttejä. Tämä vuorovaikutus aiheutuu pitkän kantaman dipolivuorovaikutuksesta. Vaikka nämä voimat vaikuttavat kappaleiden koko rajapinnan alueella, käytännössä vaikutus rajoittuu maksimissaan muutamien satojen nanometrien kokoisiin saarekkeisiin pintojen pienten epätasaisuuksien vuoksi. Tämän vuoksi dipolivuorovaikutuksella on merkitystä lähinnä korkeintaan mikrometrien kokoluokkaa olevien kappaleiden välillä.

Tämä työ koostuu kahdesta osasta. Ensimmäisessä osassa pinnan vuorovaikutuksia on tutkittu ultratyhjiöolosuhteissa mallipinnan avulla ja toisessa normaaliolosuhteissa käyttäen realistisia pintoja.

Bentseenin adsorptiorakenne Co(0001) pinnalla määritettiin kokeelisesti käyttäen matalaenergisten elektronien diffraktiota. Kokeellisten tulosten lisäksi käytettiin tiheysfunktionaaliteoriaan perustuvaa mallinnusta. Tutkimus paljasti kaksi mahdollista adsorptiorakennetta eri lämpötiloissa. Saturaatiopeitoksi saatiin 0.143 kerrosta. Tarkempi analyysi paljasti bentseenirenkaan makaavan pinnan hcp-paikalla lappeellaan hiili–vety -sidokset hieman pinnalta pois päin taipuneina.

Pienten hiukkasten tarttumista pintoihin tutkittiin suorin, atomivoimamikroskoopilla suoritetuin voimamittauksin. Pinnan epätasaisuuksilla havaittiin olevan suuri merkitys hiukkasten tarttumislujuuteen. Erityisesti hiukkasten koko verrattuna pinnanmuotojen dimensioihin on määräävässä asemassa. Hiukkasen ja epätaisen pinnan välisen voiman arviointiin kehitettiin uusi malli, joka ottaa huomioon pinnan epäideaalisuudet. Ilman kosteuden vaikutusta hiukkasen ja pinnan väliseen vuorovaikutukseen tutkittiin laskennalisin ja kokeellisin menetelmin. Kosteasta ilmasta tiivistyy vettä hydrofiilisille pinnoille. Tällöin hiukkasen ja pinnan väliseen rajapintaan muodostuu nestesolu, joka muuttaa hiukkasen ja pinnan välistä vuorovaikutusta varjostaen dipolivuorovaikutusta ja tuoden mukaan uuden, pintajännityksestä aiheuttuvan komponentin. Hiukkasen koko ja muoto sekä pinnan geometria määräävät millainen näiden välisen voiman kosteusriippuvuus on.

Preface

This thesis has been prepared in the Surface Science group in the Laboratory of Physics at the Helsinki University of Technology during the years 2002–2006. I am grateful to Prof. Pekka Hautojärvi for giving me the opportunity to work in this experimental group.

I wish to express my gratitude to Docent Jouko Lahtinen for the expert guidance and supervision he has provided during the time I have been in the laboratory. I also want to thank Dr. Adam Foster for encouraging me at times I needed it. My co-workers Karin Habermehl-Ćwirzeń, Matti Paajanen and Olli Pakarinen deserve special thanks for working with me. Our discussions have been the most fruitful. The help from the technical and administrative staff in the laboratory is appreciated. I also wish to thank all my collaborators at Helsinki University of Technology, University of Helsinki and VTT. The financial support from TEKES is gratefully acknowledged.

I want to thank people around the coffee table in the Laboratory of Physics for not so scientific conversations. Very special thanks belongs to the former and current members of the laboratory Lauri Salminen, Jaani Nissilä, Jani Sainio, Mikko Aronniemi, Matti Paajanen and Eija Järvinen. My friends in the Laboratory of the Round Table deserve to be thanked for the enjoyable lunch hours.

I am deeply indebted to my parents for their support during my whole life. My sister Erja has been a valuable pacesetter which is greatly appreciated. My brother Ville earns special thanks for the time spent with me. It has definitely been entertaining.

Finally, I would like to thank Driving school's president Veikko Sompa and his students.

Espoo, December 2006

Jukka Katainen

Contents

List of publications

This thesis consists of an overview and the following publications:

I K.M.E. Habermehl-Ćwirzeń, J. Katainen, J. Lahtinen, and P. Hautojärvi, *An Experimental Study on Adsorption of Benzene on Co(0001)*, Surface Science **507-510**, 57-61 (2002).

II K. Pussi, M. Lindroos, J. Katainen, K. Habermehl-Ćwirzeń, J. Lahtinen, and A.P. Seitsonen, *The* $(\sqrt{7} \times \sqrt{7})R19.1°$*-*$C_6H_6$ *Adsorption Structure on Co(0001): a Combined Tensor LEED and DFT Study*, Surface Science **572**, 1-10 (2004).

III J. Katainen, M. Paajanen, E. Ahtola and J. Lahtinen, *Adhesion as an Interplay Between Particle Size and Surface Roughness*, Journal of Colloid and Interface Science **304**, 524-529 (2006).

IV O.H. Pakarinen, A.S. Foster, M. Paajanen, T. Kalinainen, J. Katainen, I. Makkonen, J. Lahtinen, and R.M. Nieminen, *Towards an accurate description of the capillary force in nanoparticle-surface interactions*, Modelling and Simulation in Materials Science and Engineering **13**, 1175-1186 (2005).

V M. Paajanen, J. Katainen, O.H. Pakarinen, A.S. Foster and J. Lahtinen, *Experimental Humidity Dependency of Small Particle Adhesion on Silica and Titania*, Journal of Colloid and Interface Science **304**, 518-523 (2006).

The author has had an active role in all phases of the research reported in this thesis. He is responsible for the LEED experiments and interpretation of the results in publication I. He has performed all the experiments in publication II. He has participated in planning and performing the experiments in publications III–V. The author has contributed in the writing of all the publications and been the responsible author of the publication III.

Chapter 1

Introduction

Surfaces play an active role in many applications ranging from molecular level to macroscopic phenomena. On a molecular level surface bonds are utilized *e.g.* in catalysis, sensor applications and coating technology. Bonds in the molecular level are usually formed between single atoms with very limited interaction range originating from the charge transfer between the species. On the macroscopic side, surfaces or interfaces between bulk objects have interaction even when the surfaces are inert in the chemical sense. The interaction is caused by a long range electrostatic forces acting on the whole interface. However, this interaction is significant only for particles around 100 μm or below in diameter. For larger particles gravitational and inertial effects dominate and the roughness present on all practical surfaces further reduces the significance of the surface forces even for particles in the micrometer range.

Catalysts are widely used in chemical industry. The reason is evident: catalysts reduce the activation energy of the reaction, speed them up, change the balance in the reaction towards the products, etc. Catalysts are also used in exhaust gas cleaning since they enable conversion of toxic gases, such as CO, to less harmful compounds for example in automobiles and power plants. However, detailed knowledge of the catalytic behavior of many systems is unknown. Due to the complexity of the catalytic systems, studies of the operation of a real catalyst are very demanding. Thus, in order to gather understanding of the catalytic processes, simplified model systems have to be used. Surface studies using well defined surfaces and ultra high vacuum conditions is a way to understand at least some of the aspects in the catalytic processes.

In publications I and II the adsorption of benzene on a cobalt single crystal surface has been studied. The bonding of aromatic compounds plays an important role in many catalytic processes. Benzene, the simplest aromatic molecule, can be

used as a model for more complicated aromatics. The understanding of the adsorption of benzene gives new information on the reactions in which aromatic hydrocarbons are involved.

Adhesion of small particles onto surfaces is utilized in many ways in industrial applications. For example in the coating industry it is used to produce thick film structures for sensor applications and fiber optics preforms. The drawbacks of the adhesion can be seen *e.g.* in energy production. Combustion of liquid or solid fuel yields small ash particles in the exhaust gas. The ash deposition on the heat exchanger surfaces reduce the efficiency and leads to the need to either clean or replace the surfaces.

With inhalable drugs the picture is slightly different. In inhalators very small drug particles have to be used since the natural defense system of the respiratory organs prevent inhaling large particles. However, the small particles easily form agglomerates too large to be inhaled. The solution is to adhere the drug particles onto the surfaces of carrier particles large enough not to form agglomerates. Turbulent flow inside the dosing device is used to separate the drug from the carriers when inhaled. The inhaling of the carriers is blocked by the defense system while the drug particles are able to enter the lungs. Studying the adhesion properties using model systems leads to more intimate understanding of the features behind the adhesion giving us more tools to control the adhesion in real applications.

In publication III the adhesion of small particles on rough surfaces has been studied. Even very low surface roughness reduces the adhesion significantly. Since the surfaces in the real applications are seldom atomically smooth, the surface roughness has to be considered in almost all practical applications where small particles are likely to deposit onto surfaces. Of particular interest has been the size of the particles relative to the dimensions of the surface features.

In publications IV and V the effect of ambient humidity on adhesion has been studied. In humid conditions a capillary bridge forms between the particle and the surface increasing the adhesion when the surfaces are hydrophilic. The bridge changes the nature of the adhesion from van der Waals type to surface tension induced adhesion, which usually increases the strength of adhesion. The effect of humidity has been studied using numeric simulations as well as experiments considering different particle–surface geometries.

Chapter 2

Experimental methods

2.1 Low energy electron diffraction

Low energy electron diffraction (LEED) [1] is a technique frequently used in examining single crystal samples and adsorbed adlayers. It provides useful information on the symmetry and atomic structure of the adlayers as well as on the relaxations of the substrate atoms in three dimensions.

In a LEED experiment electron beam with energy between 20–500 eV is focused to the sample surface. The electrons scatter from the topmost atomic layers due to the short mean free path of electrons in solids. Since the wavelength of an electron in this energy range is similar to the interatomic spacing in solids, the backscattered electrons exhibit a diffraction pattern which gives information on the surface structure. The backscattered electrons are collected on a fluorescent screen where the diffraction pattern may be observed. Fig 2.1 shows a schematic picture of the LEED apparatus. The negative bias $-E_k + \Delta V$ in the grids G_2 and G_3 prevent inelastically scattered electrons reaching the screen while surrounded by grounded grids G_1 and G_4. The adjustable potential ΔV is in the range of few volts and is used to optimize the contrast of the diffraction pattern on the screen.

The diffraction pattern observed as spots on the fluorescent screen presents the reciprocal lattice of the sample. Fig. 2.2 shows an example of a LEED image recorded from a clean Co(0001) surface and a schematic presentation of the diffraction pattern. Since the diffraction is not fully two dimensional, but includes several atomic layers, the third dimension may be probed by scanning the beam energy. In this method, called IV-analysis, the intensities of the diffraction spots are recorded as a function of the beam energy. For maximal reliability, as many spots with as wide energy range as possible are used.

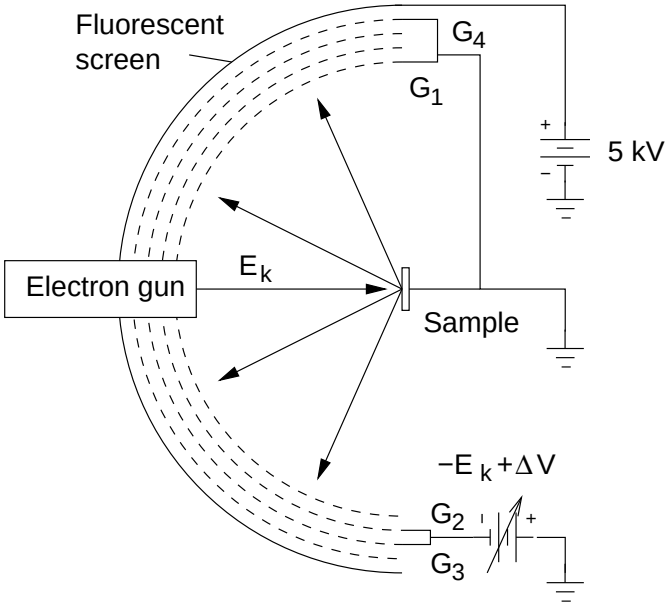

Figure 2.1: A schematic view of the LEED apparatus.

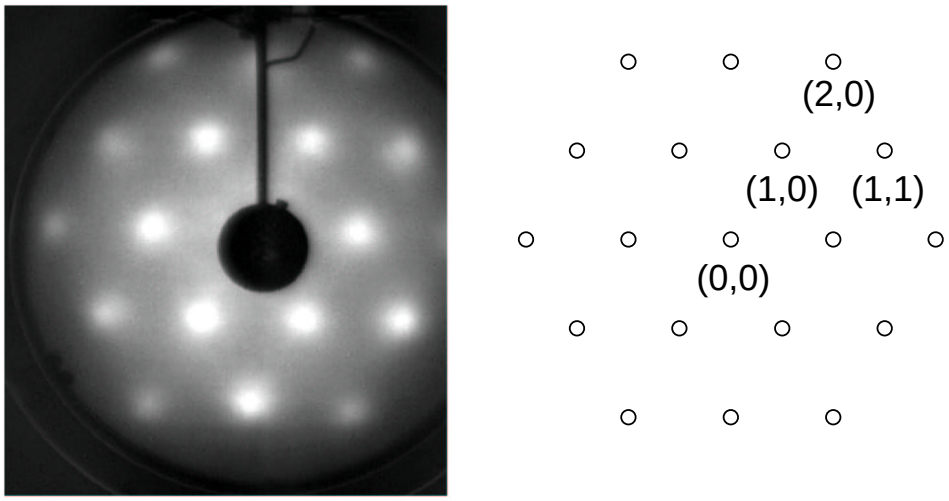

Figure 2.2: LEED pattern recorded from a Co(0001) surface (electron beam energy 346 eV). The schematic picture on the right shows indexing of the spots.

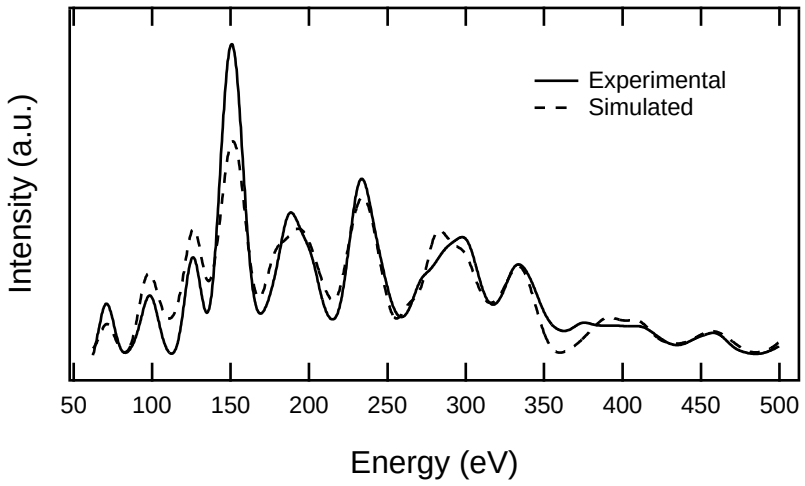

Figure 2.3: Comparison of experimental and simulated IV-curve. Spot (1,0) from a Co(0001) surface.

In IV-analysis theoretical IV-curves are simulated by quantum mechanical calculations. Theoretical curves calculated from an initial structure are compared to the experimental ones. The assumed structure is refined and the resulting curves are again compared to the experiments. The iteration is continued until the best fit is obtained [2, 3]. Fig. 2.3 shows a comparison between an experimental and simulated IV-curve for a Co(0001) surface.

The comparison of the measured and calculated curves utilizes so called reliability factors that take into account position, height and the width of the peaks, weighting the position since the peak intensities are difficult to predict. The Pedry's R-factor (R_P) [4] is the most used reliability factor.

2.2 Scanning force microscopy

Scanning probe microscopies have opened a new world into imaging of small objects. Since the invention of the Scanning Tunneling Microscopy in 1981 [5] various new techniques based on the same idea have been introduced. The main spin off is the scanning force microscopy (SFM) first demonstrated by Binnig *et al.* in 1986 [6].

Fig. 2.4 shows a schematic view of a SFM apparatus. The motion of the cantilever is detected by a laser and a photodiode. The resulting signal is used by various feedback circuits depending on the operating mode. The feedback circuits keep the interaction between the sample and the tip constant by moving the surface

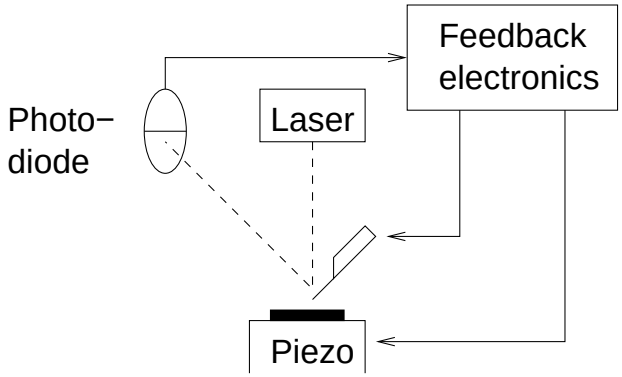

Figure 2.4: A schematic view of a SFM apparatus.

vertically during the lateral scanning. Combining the recorded vertical and lateral movements the height profile of the surface is obtained. Small movements needed are created using piezo crystals.

SFM may be used in three operating modes: In the contact mode the tip is gently pressed against the sample surface and the feedback keeps the deflection of the cantilever constant. In ideal conditions this mode is capable of reproducing the periodicity of the surface lattice, but true atomic resolution *i.e.* point defects *etc.* cannot be detected. Soft samples may also be damaged during the scanning.

In the non-contact mode [7] the cantilever is vibrated at a constant amplitude near its resonance frequency above the sample surface. The change in frequency, due to interaction between the sample and the tip, is used as a feedback signal. The non-contact mode is capable of imaging in true atomic resolution. Non-contact mode may be used only in vacuum conditions. [8]

In the amplitude modulating (or Tapping) mode the cantilever is also vibrated near its resonance frequency. The tip is brought so close to the surface that it touches the surface in the lowest point of each oscillation cycle, *i.e.* it "taps" the surface. This method of imaging is faster than the contact mode and not as destructive. The phase shift of the oscillating cantilever gives additional information on the chemical and mechanical properties of the sample. This is the prevailing mode used for topography imaging in ambient conditions. [9]

The SFM can also be used to measure forces between particles and surfaces [10, 11]. In force measurements the particle is glued to the cantilever in place of the tip. The particle is brought into contact with the surface and the movement is reversed. The particle stays in contact until the spring force of the deflected cantilever exceeds the adhesion. At this moment the particle detaches from the surface and the cantilever returns to its neutral position. Fig. 2.5 presents a typical deflection curve obtained from a force measurement. Using the spring constant

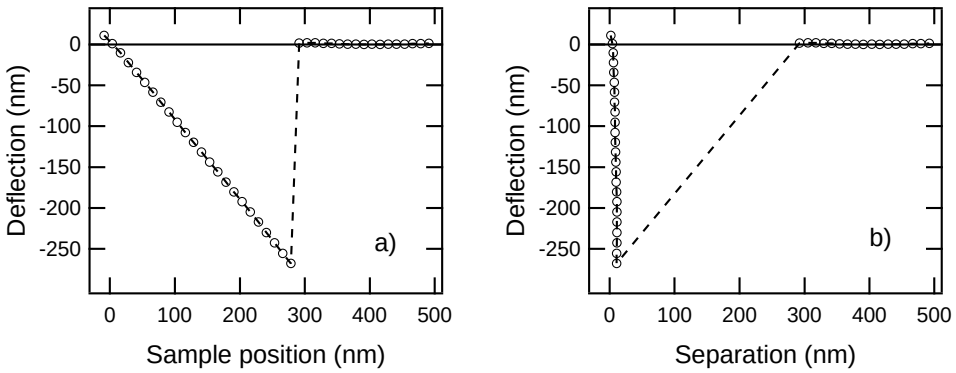

Figure 2.5: Typical deflection curve obtained from a force measurement as a function of a) sample position and b) particle–surface separation. The particle stays in contact with the surface until the spring force of the deflected cantilever exceeds the particle–surface adhesion.

of the cantilever, the deflection may be converted to force. The maximum deflection corresponds to force needed to separeate the probe from to surfaces, *i.e.* the pull-off force.

Since the surfaces are seldom atomically smooth, the pull-off force has to be measured at several locations on the surface in order to achieve statistically reliable results. In some cases this means hundreds of single measurements resulting in force distributions rather than single values. Fig. 2.6 shows an example with experimental data from two surfaces. Although broad scatter of the pull-off force is evident, the distributions have clear maxima which may be used as the representative values.

2.3 Other spectroscopies used in this work

Thermal desorption spectroscopy (TDS) is a simple method to obtain information on the species adsorbed on surfaces. Initially, the surface is prepared by exposing it to the gas wanted to be adsorbed. In a TDS experiment the sample is heated at a constant rate and the partial pressures of the residual gases in the vacuum chamber are monitored, usually with a mass spectrometer. The increase in thermal energy leads to desorption of the adsorbed species or their fragments. The desorption is detected as a rise in the partial pressure of the compound. Information on *e.g.* the adsorption kinetics, the number of different adsorption sites and the amount of adsorbed species may be obtained from the desorption

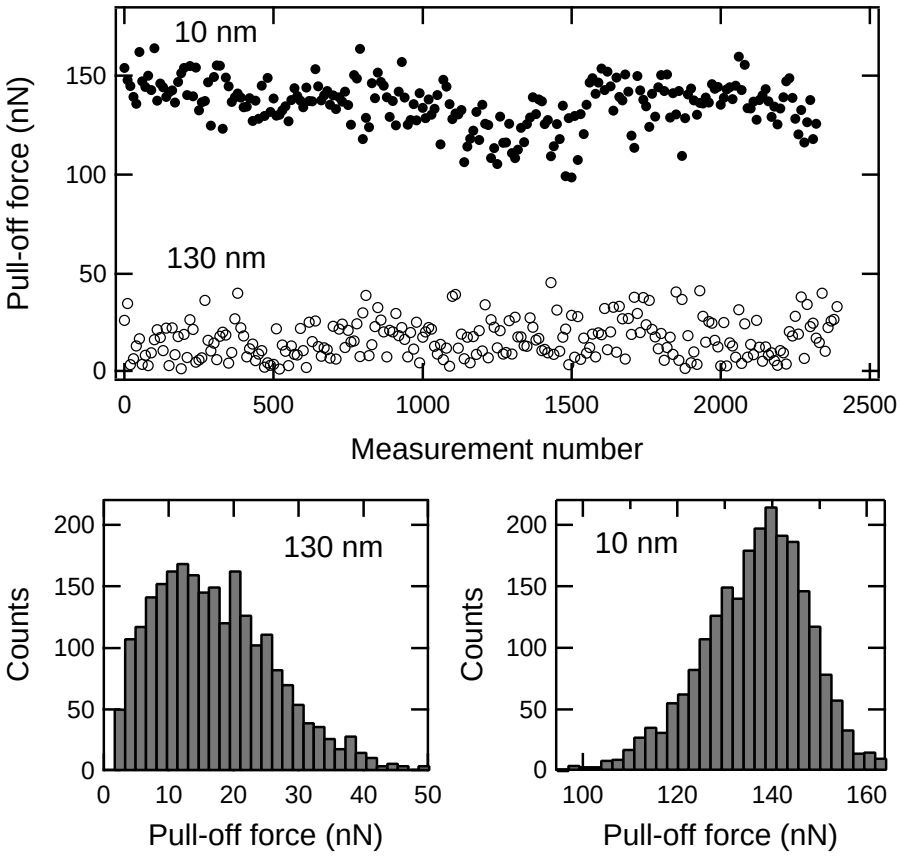

Figure 2.6: Pull-off forces and resulting force distributions measured on 10 nm coating (•) and 130 nm coating (◦). The thicker coating is much rougher. For clarity, only every tenth measurement point is shown in the upper picture.

spectra. [12]

X-ray photoelectron spectroscopy (XPS) is a surface sensitive method which utilizes the photoelectric effect. The sample is bombarded with X-rays and the binding energy spectrum of the electrons emitted from the sample is recorded. The spectrum reveals the chemical composition of the surface and, if high resolution can be used, information on the chemical state of the elements is obtained. XPS may also be utilized to determine the work function of the sample. [13]

Chapter 3

Adsorption structure of benzene on Co(0001)

The adsorption of benzene on metallic surfaces is of considerable interest because it serves as a model system for more complicated cyclic hydrocarbons. The bonding of aromatic hydrocarbons plays an important role in many catalytic processes. Determination of the detailed adsorption geometry of the benzene molecule is, therefore, of fundamental importance.

The main issues discussed in the literature have been the magnitude of substrate induced distortions on the benzene molecule and the effect of the neighboring molecules on the choice of the adsorption site and orientation. Studies of surface structures, which have mostly been done on hexagonal close packed surfaces, indicate flat lying, π-bonded molecular adsorption with a small increase in the diameter of the carbon ring along with small Kekulé type distortions and possible benzene induced substrate distortions [14–20].

In publications I and II the adsorption of benzene on Co(0001) surface has been studied.

3.1 Adsorption of benzene on Co(0001)

The adsorption of benzene was studied using LEED, TDS and XPS, LEED being the main technique. Benzene was found to form two adsorption structures: At room temperature a $c(2\sqrt{3} \times 4)rect$ structure was detected. A LEED image and the corresponding schematic presentation of the diffraction spots are presented in Fig. 3.1. The schematic picture shows that there are three domains present due to possible orientations of the adlayer relative to the substrate. The real space

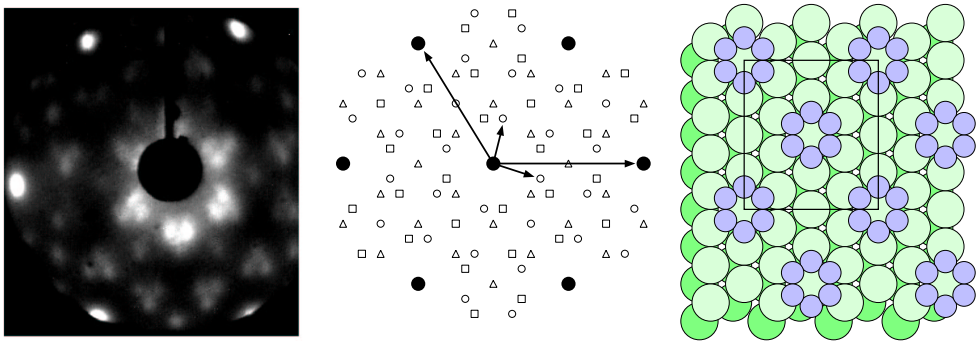

Figure 3.1: Observed and schematic $c(2\sqrt{3} \times 4)rect$ LEED pattern of benzene adsorbed on Co(0001) at room temperature (66 eV) and corresponding structure in real space.

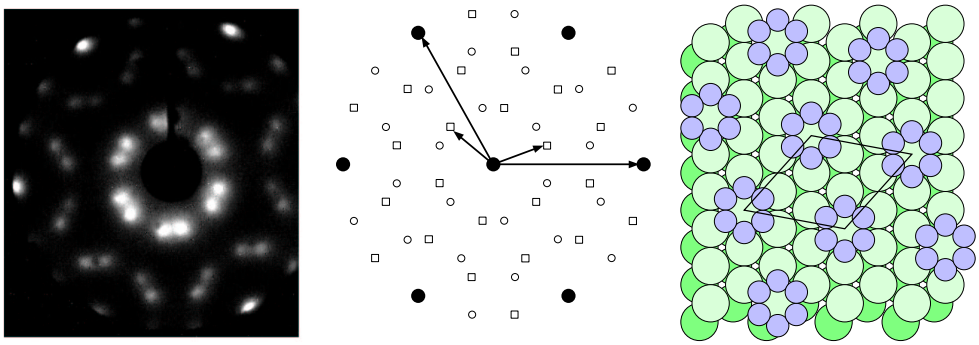

Figure 3.2: Observed and schematic $p(\sqrt{7} \times \sqrt{7})R19°$ LEED pattern of benzene adsorbed on Co(0001) at 220 K (62 eV) and corresponding structure in real space.

structure is also presented in Fig. 3.1 showing the two molecules in the overlayer unit cell. This structure was detected with wide range of room temperature exposures. The second structure, $p(\sqrt{7} \times \sqrt{7})R19°$, was detected when benzene was adsorbed below 220 K with high exposures. The resulted LEED pattern, with two domains, and the structure are shown in Fig. 3.2. The overlayer is rotated 19.1° relative to the substrate. Coverages for these structures are 1/8 and 1/7, correspondingly.

In the TDS measurements only desorption of H_2 was observed indicating that benzene partly dehydrogenates during heating. Fig. 3.3 shows TD spectra measured for exposures between 4 and 25 L. The amount of hydrogen desorbed [21] suggests that only one hydrogen atom desorbs leaving C_6H_5 hydrocarbon fragment on the surface. A similar process was also suggested for Os(0001) [22] and

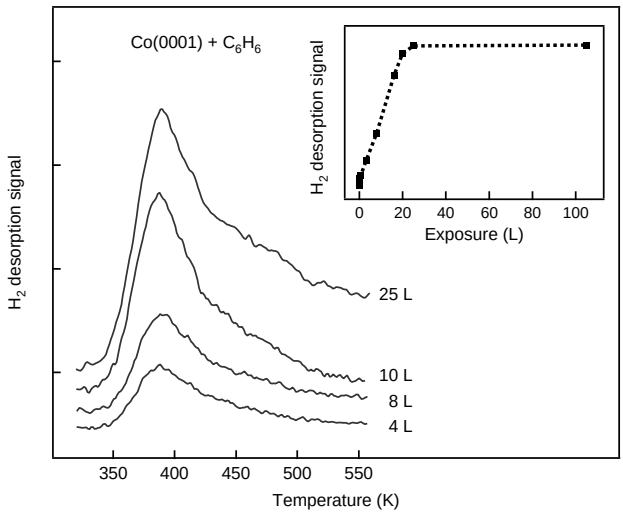

Figure 3.3: Thermal desorption spectra obtained after exposing a clean Co(0001) surface to benzene. The exposure was varied between 4 and 25 L. The inset shows the H_2 desorption signal as a function of benzene exposure. The line is drawn to guide the eye.

Co($10\bar{1}0$) [23, 24].

With increasing coverage there is no temperature shift visible in the desorption-peak maximum indicating a first-order process. This behavior suggests that the decomposition process might be the limiting step of the desorption. The activation energy of the decomposition was estimated to 102 kJ/mol. This value is almost the same as suggested for the dehydrogenation of benzene on Co($10\bar{1}0$) [24].

3.2 Analysis of the $p(\sqrt{7} \times \sqrt{7})R19.1°$-$C_6H_6$ adsorption structure

The saturation structure $p(\sqrt{7} \times \sqrt{7})R19.1°$-$C_6H_6$ was chosen to be analyzed in detail. IV-curves for three integral and seven fractional order beams were measured with cumulative energy range of 1470 eV. The multilayer relaxation and reconstruction of benzene-covered cobalt surface was analyzed using Tensor LEED codes of Van Hove *et al.* [25]. The comparison between the experiment and the theory was done using Pendry R-factor and the error bars quoted are calculated using the Pendry RR-function [4].

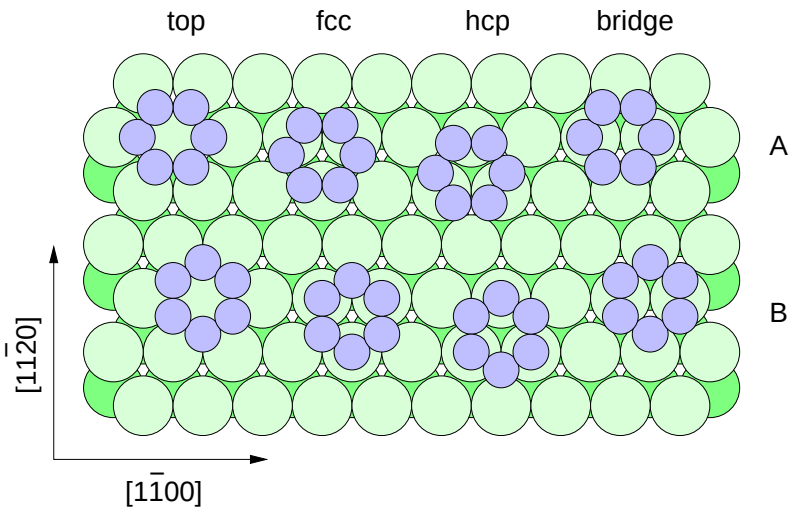

Figure 3.4: High symmetry adsorption sites. Main crystallographic directions are indicated with arrows. Carbon atoms and the two top cobalt layers are shown.

There were eight possible high-symmetry adsorption sites to be considered: two top sites, two hcp sites, two fcc sites and two bridge sites. The two different high symmetry orientations of the benzene molecule are the two parallel C–C bonds aligned with [1$\bar{1}$00] direction (A) and with [11$\bar{2}$0] direction (B). These sites are shown in Fig. 3.4.

The LEED investigation revealed that the benzene molecule is adsorbed on a hcp A site with a final Pendry R-factor value of 0.26. Fig. 3.5 compares the experimental IV-curves to the theory. The agreement is excellent for the integral order beams. The Pendy method is not sensitive to the relative intensities of the beams. Fig. 3.5 also shows a schematic picture of the diffraction pattern where the indexes of the beams used in this analysis are shown. Two different domains that are related to each other by a mirror plane along [11$\bar{2}$0] direction are shown with different symbols (∘,□).

The adsorption of benzene on Co(0001) was studied also with density functional theory (DFT) calculations, performed in the Kohn–Sham formalism, with the generalized gradient approximation (GGA) of Perdew et al. [26] as the exchange-correlation functional. In the calculations the adsorption at all the sites except bridge B was investigated. The bridge B site was not studied, because the adsorption energy of bridge A was about 0.25 eV higher than at the hcp A and fcc A, which represent the energetically lowest and practically degenerate adsorption sites. However, since the LEED experiment unambiguously prefers the hcp A site, it was concentrated on.

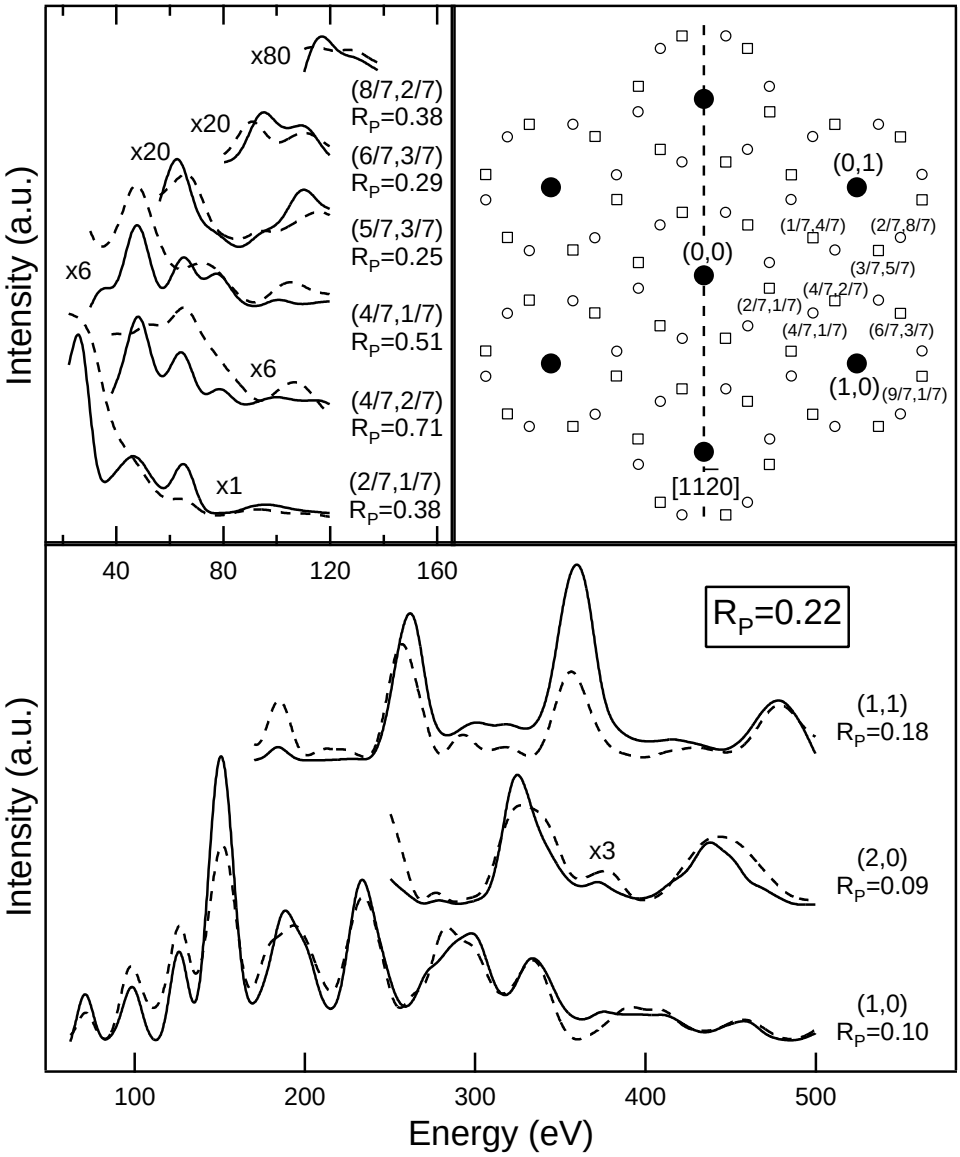

Figure 3.5: Theory–experiment comparison. Dashed line corresponds to the theory and solid line to the experiment. Right upper corner shows schematically the diffraction pattern with the indexes indicating the beams used in this calculation. The two different domains that are related by a mirror plane along [11$\bar{2}$0] are marked with different symbols (∘, □).

Table 3.1: The main geometric parameters with the associated errors obtained with the LEED and DFT–GGA calculations.

Overlayer			Substrate		
Parameter	Value (Å)		Parameter	Value (Å)	
	LEED	DFT–GGA		LEED	DFT–GGA
C–Co	2.26 ± 0.09	2.104	Δ_1	0.09 ± 0.06	0.191
$dz_{\mathrm{C-Co}}$	2.20 ± 0.09	1.964	Δ_2	0.01 ± 0.09	0.036
C–C	1.39 ± 0.10	1.446	Δ_3	0.01 ± 0.07	-0.017
H–C	1.1 ± 0.2	1.091	Δ_4	0.0 ± 0.3	-0.082
$dz_{\mathrm{H-C}}$	0.3 ± 0.2	0.392	dz_{12}	2.03 ± 0.10	1.989
Δ_{C}	0.01 ± 0.11	0.0	dz_{23}	2.09 ± 0.10	2.024
Δ_{H}	0.04 ± 0.4	0.0	dz_{34}	1.97 ± 0.10	1.999

Different parameters can be identified with the help of Fig. 3.6. In the DFT–GGA results the negative sign indicates that the relaxation occurs in the opposite direction with respect to the relaxation produced by the LEED calculation.

The main geometric parameters resulting from the both utilized methods are shown in Table 3.1. The parameters can be identified with the help of Fig. 3.6 where the part a) shows the top view and part b) the side view of the optimal geometry.

The results imply relatively weak interaction between the substrate cobalt and the carbon in the benzene. The shortest C–Co bond was found to be 2.26 ± 0.09 Å with LEED and 2.104 Å with DFT, compared to 2.04 Å, which is the sum of the metallic radius of cobalt and the covalent radius of carbon in single bond. The carbon ring remains nearly unchanged (LEED) or slightly expanded (DFT) with respect to the gas phase value of the C–C bond of 1,399 Å [27], with negligible buckling (Δ_C). Carbon–hydrogen bonds are slightly expanded compared to the C–H bond in the gas phase benzene (1.08 Å). Buckling between the hydrogen atoms (Δ_H) is within the error of the analysis. The carbon–hydrogen bonds are bent away from the surface, hydrogen atoms lying higher than the center of mass of the carbon ring according to both techniques.

Benzene induces some changes to the substrate structure. LEED studies indicate that the first interlayer spacing (z_{12}) remains similar to the bulk value. The second (dz_{23}) interlayer spacing is expanded by 3% and the third (dz_{34}) interlayer spacing is contracted by 3%. The DFT calculations give a slightly different picture with interlayer spacings closer to the bulk value. The interlayer spacings are quoted between the centers of mass of the layers. Large buckling was found for the first cobalt layer: 0.09 Å (LEED) and 0.19 Å (DFT). The buckling found by DFT is noticeably larger than found in the LEED analysis. The buckling in the first

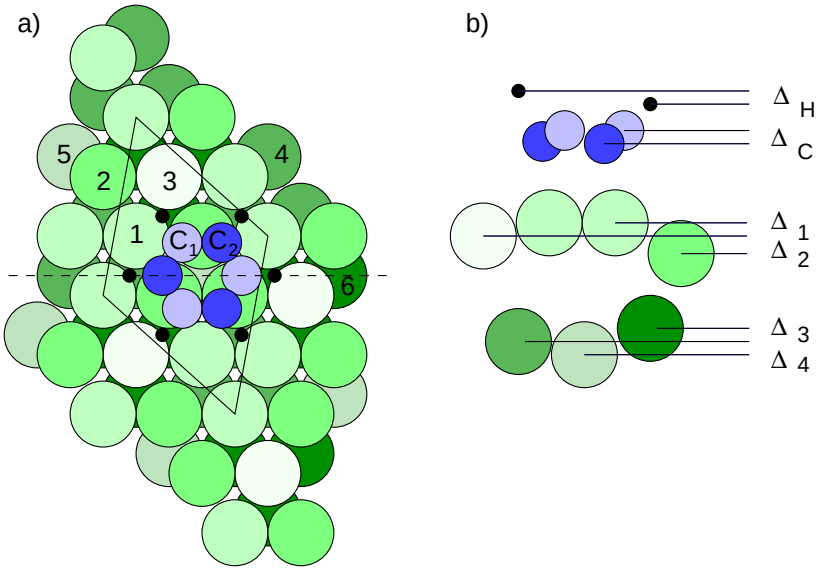

Figure 3.6: a) Top and b) side views of the favored geometry calculated by LEED. Dashed line indicates the $[1\bar{1}00]$-direction. p($\sqrt{7} \times \sqrt{7}$) unit cell is shown with a solid line. The inequivalent Co atoms in the first two layers and the C atoms are indicated by different numbers.

substrate layer has been qualitatively different in the various DFT calculations published so far: at Ru(0001) [28] the buckling is in the range of 0.03 Å and at Ni(111) and Pt(111) around 0.15–0.20 Å [29–31], whereas in the experiments it has always been small. Because of the strong buckling in the first layer, interlayer spacings do not give a realistic picture about the situation between the first two cobalt layers. LEED investigation implied that the cobalt atoms right below the benzene ring (atom 2 in Fig. 3.6 a)) are pulled up by 0.10 ± 0.06 Å compared to the center of mass of the other atoms in the first layer (atoms 1 and 3 in Fig. 3.6 a)), which are almost planar.

The DFT calculations resulted in a work function of 5.05 eV for the clean Co(0001) surface and 3.38 eV for the surface covered with the benzene, whereas experiments showed values of 5.55 eV [32] and 4.25 eV, respectively. The reductions in work functions as a result of benzene adsorption were 1.77 eV for the DFT calculations and 1.30 eV for the experiment.

Chapter 4

Adhesion of small particles

Deposition of small particles onto surfaces is of significant importance in a large number of applications. For example ash particle deposition on heat exhanger surfaces is a problem in energy production. The deposited porous layer of ash particles reduces the capacity of the exhanger leading ultimately to the need to either clean or replace the active surfaces. In addition to the capacity problems, the deposited particles accelerate corrosion by providing sites for condensation of corrosive substances.

In the literature the adhesion of small particles is widely studied using force measurements, for a review see [10, 11]. The surface roughness has been detected to reduce the adhesion significantly [33–35]. In order to explain experimentally observed adhesion on rough surfaces, both analytical [36–38] and computational [39–41] approaches have been used. While computational methods produce a good agreement with the experiments [41, 42] they are complex and thus not easily applied for fast estimation of the adhesion for specific systems. On the other hand, analytical equations rely only on a few parameters which are easily determined from the surface topography. This ensures that they can be easily used for multiple systems to estimate the adhesion [43, 44].

The adhesion of small particles has been demonstrated to be dependent on the ambient humidity and the hydrophobicity of the materials [45–50]. Surface roughness has also been seen to play a role in capillary formation [51–53]. The very complex nature of the humidity dependence has been studied by simplified models [54–59]. However, when the size of the particle decreases, these models do not necessarily provide correct estimates for the capillary forces.

In publications III-V adhesion of small oxide particles on oxide surfaces has been studied. Publication III concentrates on adhesion on rough surfaces and publications IV-V on the effect of humidity on adhesion.

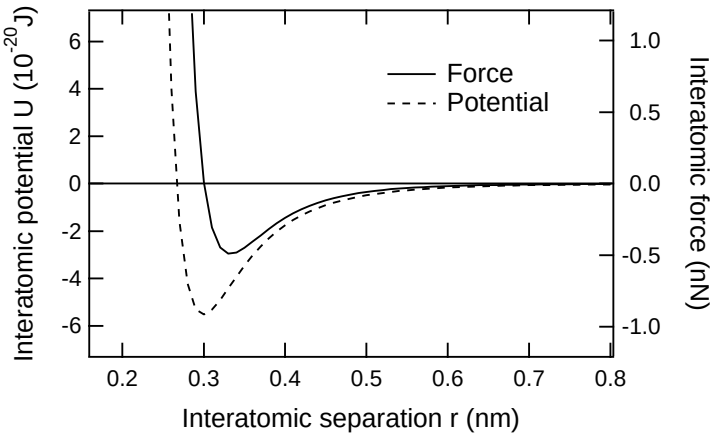

Figure 4.1: *Lennard–Jones* potential and force calculated for silver atoms as a function of interatomic separation r. ϵ=55.3 zJ and σ=2.64 Å [61].

4.1 Principles of adhesion

Adhesion between neutral particles originates from intermolecular interactions called *dispersion forces* [60]. This interaction may be understood by considering an atom as a positively charged nucleus surrounded by a negatively charged electron cloud. Although atom or molecule may not have permanent dipole moment, it has an instant dipole moment due to the movements of the electron cloud. This dipole induces dipole moments to the nearby atoms leading to attractive interaction between the atoms. The interaction is described by *van der Waals* potential which decays as r^{-6} for interparticle separation r. If the atoms get too close to each other, electron clouds start to overlap leading to a repulsive interaction. With the semi-empirical term for repulsion the interaction between two neutral atoms may be written as a *Lennard–Jones* potential [60]

$$U(r) = 4\epsilon \left[\left(\frac{\sigma}{r}\right)^{12} - \left(\frac{\sigma}{r}\right)^{6} \right], \tag{4.1}$$

where ϵ and σ determine the strength and the range of the interaction. Fig. 4.1 shows the *Lennard-Jones* potential and corresponding force between two silver atoms.

The interaction for macroscopic particles may be calculated by summing over all atoms in the system. Assuming continuum objects, calculations may be transformed into integrals and carried out analytically and *e.g.* for a sphere on a flat

substrate resulting in

$$F_{\mathrm{adh}} = \frac{\mathcal{A}_{\mathrm{H}} R}{6 H_0^2}, \tag{4.2}$$

where $\mathcal{A}_{\mathrm{H}}$ is the *Hamaker constant*, R the radius of the adhering sphere and H_0 the equilibrium separation between the particle and the surface. When the particle and the substrate are of different materials, the Hamaker constant can be calculated from

$$\mathcal{A}_{\mathrm{H}_{12}} = \sqrt{\mathcal{A}_{\mathrm{H}_{11}} \mathcal{A}_{\mathrm{H}_{22}}}, \tag{4.3}$$

where $\mathcal{A}_{\mathrm{H}_{\mathrm{ii}}}$ is the Hamaker constant for material i. [60]

However, this ideal approach is of very limited use since the materials are seldom perfectly smooth or circular. Eq. (4.2) is derived for rigid objects omitting all elastic behavior. Several models have been developed to include elasticity: Johnson–Kendall–Roberts (JKR) [62], Derjaguin–Müller–Toporov (DMT) [63] and Maugis [64], which all cover different elasticity ranges. Long range interactions like charging may also have significant effect on adhesion. In ambient conditions humidity also plays an important role.

4.2 The effect of surface geometry

Due to the surface roughness, present in all practical surfaces, eq. (4.2) does not predict measured forces very well. Recent models which take the surface roughness into account are based on approach where the asperities are assumed to be hemispherical caps on a smooth substrate [36]. Rabinovich *et al.* [37,38] have suggested that the adhesion on surfaces exhibiting asperities should be written as a combination of sphere–sphere and sphere–surface interactions in the form

$$F_{\mathrm{adh}} = \frac{\mathcal{A}_{\mathrm{H}} R}{6 H_0^2} \left[\frac{r}{r + R} + \frac{1}{(1 + y_{\max}/H_0)^2} \right], \tag{4.4}$$

where R is the radius of the adhering particle, H_0 the equilibrium distance, r the radius of the asperity on the surface and $y_{\max}$ the height of the asperity. The first term is the adhesion between the asperity and the particle, separated by H_0 and the second term the contribution of the particle–substrate interaction. Fig. 4.2 a) illustrates the contact geometry used in deriving eq. (4.4). This approach overestimates the adhesion because the last term takes the whole interacting surface into account as a plane, resulting in double counting of the contribution of the substrate under the asperity. To reduce the effect of double counting, a condition $R \gg r$ must apply indicating that the adhering particle is much larger than a single asperity.

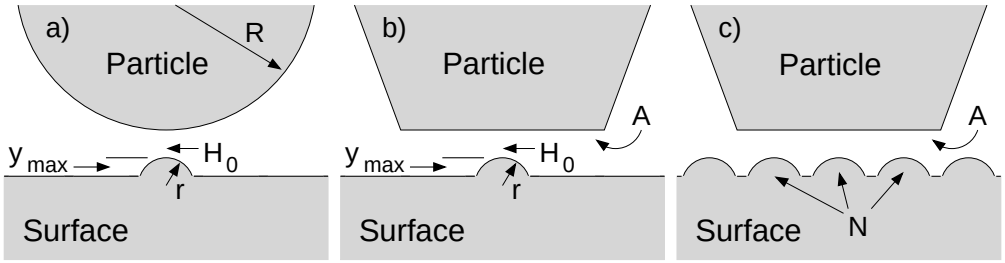

Figure 4.2: Contact geometries in different approaches a) eq. (4.4), b) eq. (4.5), and c) eq. (4.7). H_0 is the equilibrium distance between the particle and the asperity, $y_{\max}$ the height of the asperity and A the area of the particle.

The Rabinovich model, eq. (4.4), was derived for spherical particles adhering on a rough surface. Since blunt particles were used in this study, the model was modified to be suitable for blunt particles, or smooth surface, adhering to rough surfaces. The same assumptions as in deriving eq. (4.4) in ref. [37] were used, *i.e.* contact interaction with one asperity and non-contact interaction with the substrate. The geometry is shown in Fig. 4.2 b). The contact part now comes from the contact between the asperity and the flat particle and the non-contact interaction from the two parallel plates of area A. Eq. (4.4) may be rewritten for this geometry as

$$F_{\mathrm{adh}} = \frac{\mathcal{A}_{\mathrm{H}}}{6H_0^2}\left[r + \frac{A}{\pi H_0(1+y_{\max}/H_0)^3}\right], \tag{4.5}$$

where the first part is the interaction of the adhering particle with an asperity of radius r and the second part is the interaction with the substrate. In order to avoid significant double counting of the substrate eq. (4.5) is valid if the area of the adhering particle is much larger than the area of the asperity, *i.e.*

$$A \gg r^2. \tag{4.6}$$

When the measured pull-off forces are compared to forces predicted by eq. (4.5), the model clearly underestimates the adhesion with large particles. This is because the model assumes only one asperity in contact with the particle which obviously fails for large blunt particles. For particles which are of similar size or smaller than the surface features, the model gives reasonable estimates.

In order to predict the adhesion on surfaces containing features much smaller than the particles, a model which takes multiple contacts into account is needed. The number of possible contact points for a flat particle may be calculated as the average number of asperities under it, $N = A\rho$, as illustrated in Fig. 4.2 c), where

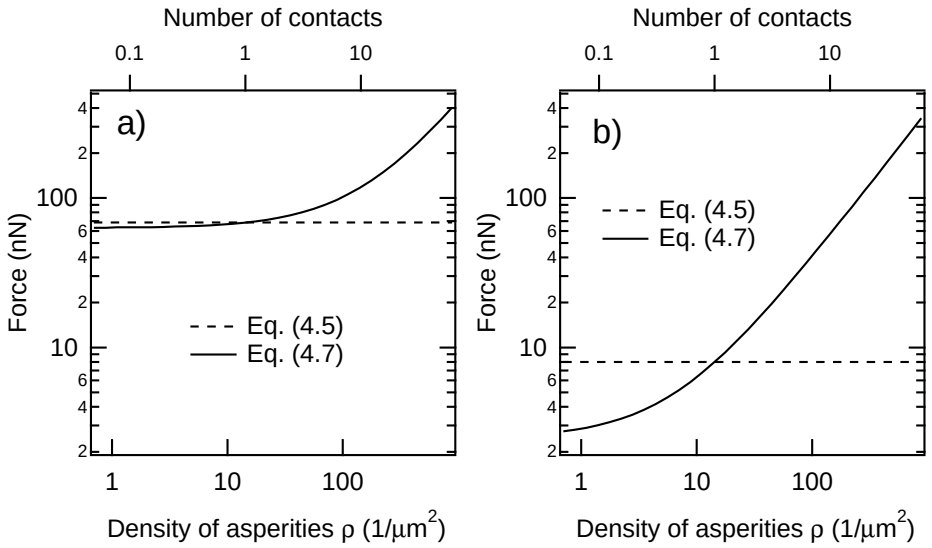

Figure 4.3: Comparison of eqs. (4.5) and (4.7) with two different asperity heights a) $y_{\max} = 1.5$ nm and b) $y_{\max} = 5$ nm. Other parameters used: $\mathcal{A}_{\mathrm{H}} = 99.1$ zJ [65], $H_0 = 3$ Å, $A = 70000$ nm^2 and $r = 30$ nm.

ρ is the density of asperities on the surface. Multiplying the contact interaction part in (4.5) by N results in

$$F_{\mathrm{adh}} = \frac{\mathcal{A}_{\mathrm{H}} A}{6H_0^2}\left[\rho r + \frac{1}{\pi H_0 (1 + y_{\max}/H_0)^3}\right]. \tag{4.7}$$

Again the first part corresponds to the interaction of the adhering particle with the asperities and the second the interaction with the substrate. If the asperities are too densely packed compared to their radius of curvature, multiple counting takes place. This leads to restriction

$$\rho \ll 1/r^2, \tag{4.8}$$

which also ensures that the error produced by counting non-contact interaction twice under the asperities is negligible if the adhering particle is large. For small particles also eq. (4.6) has to be considered. These restrictions indicate that eq. (4.7) cannot be used for surfaces with densely spaced low asperities, resulting in large r and high ρ.

Fig. 4.3 compares eqs. (4.5) and (4.7). There is no dependence on the density of asperities in eq. (4.5) but the new eq. (4.7) gives increasing forces when the density of asperities is increased. This results in much higher pull-off forces when

the density of asperities is high compared to the size of the probe. If the asperities on the surface are low, as in Fig. 4.3 a), the non-contact interaction is dominating with low asperity densities and the eq. (4.7) gives reasonable estimates over the whole range. With higher asperities, as in Fig. 4.3 b), the contribution of the non-contact part is negligible and eq. (4.7) gives unphysical values with low asperity densities. In this region eq. (4.5) should be used.

Fig. 4.4 shows measured pull-off forces from different TiO_2 surfaces in one plot as a function of number of possible contacts N, together with values calculated using the combined model of eqs. (4.5) and (4.7). The calculated values do not form a smooth curve since the values depend on the experimentally determined curvatures and heights of the asperities on the surfaces. The part where $N < 1$ in fig. 4.4 means that the particle in contact is smaller than the average area covered by one asperity. Since only the apex of the asperity contributes to the interaction, N should equal one even for particles much smaller than the asperities. Eq. (4.7) leads to unphysical values in this area. Combining eq. (4.5), for $N \leq 1$ and eq. (4.7), for $N > 1$, gives excellent agreement with the experimental data measured over three orders of magnitude in the particle/asperity length scales.

4.3 Adhesion in humid conditions

In ambient conditions water condenses between the particle and the substrate forming a meniscus or a liquid capillary neck around the contact area. The nature of the interaction between the particle and substrate is strongly modified by the meniscus [60] and it results in an additional *capillary force* increasing the particle's adhesion to the substrate. The capillary force can easily be the dominant interaction in these systems since the meniscus also screens the *van der Waals* interaction.

The size of the meniscus is determined by the ambient conditions: It grows in size, until its surface curvature has decreased to a value where the rate of evaporation and condensation is in equilibrium with the ambient. The surface tension in the concave liquid–gas interface pulls the water molecules apart from each other creating a negative Laplace pressure inside the meniscus. The Laplace pressure pulls the wetted areas of the particle and the substrate towards each other, resulting in the *capillary pressure force*. There is also a direct surface tension component in the capillary force since the surface tension in the liquid/gas interface pulls the particle and the substrate together. This force is called the *surface tension force*. [60]

Previous studies of particle–surface interactions have generally assumed that the particle is spherical, and also applied restrictions to the meniscus shape. In order

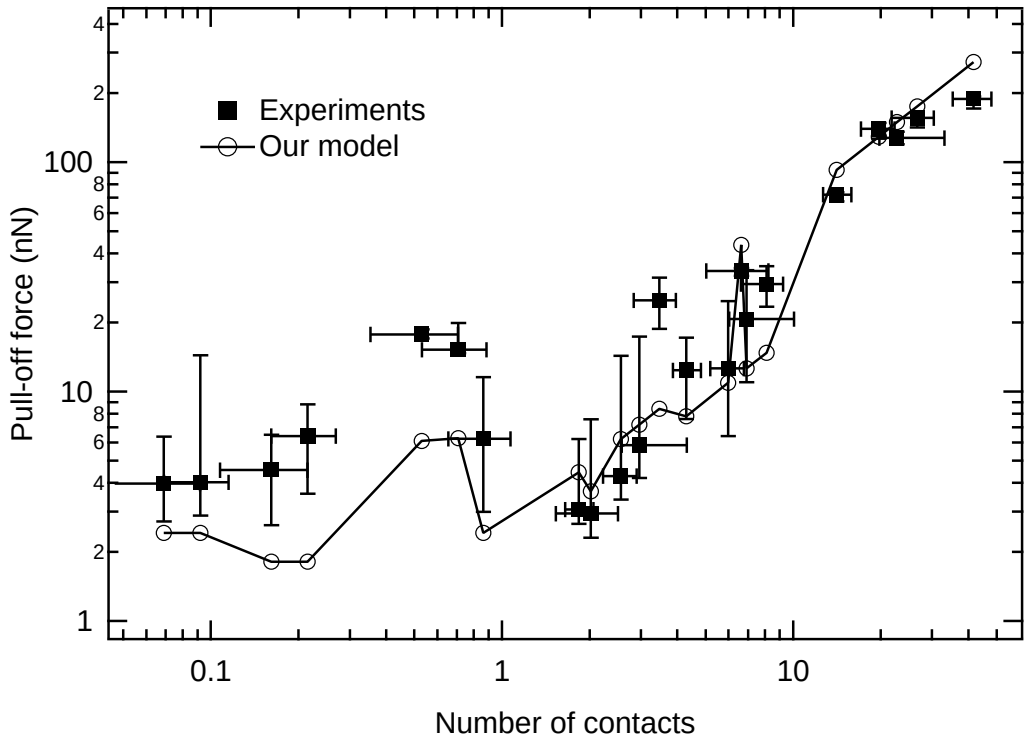

Figure 4.4: All experimental values collected and compared to our combined model using eqs. (4.5) and (4.7). The solid line is to guide the eye only.

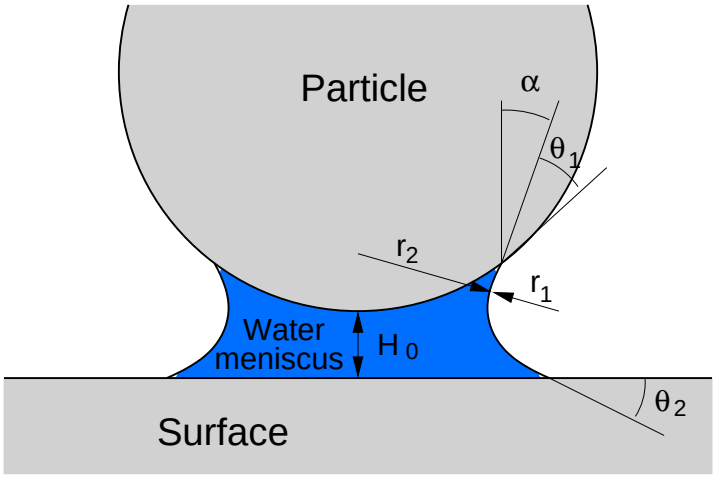

Figure 4.5: Schematic diagram showing the meniscus formed between a particle of radius R at a distance of H_0 from a surface. r_1 is the vertical radius of curvature, r_2 is the symmetry radius of curvature, θ_1 is the particle contact angle and θ_2 is the surface contact angle.

to model other particle shapes, a model for any axially symmetric shape was developed. In addition, the model makes no assumptions for the meniscus profile but calculates the exact meniscus profile where in all points of the profile the total radius of curvature is correct [60]

$$r = \left(\frac{1}{r_1} + \frac{1}{r_2}\right)^{-1}. \tag{4.9}$$

Here r_2 is the positive radius of curvature around the center axis of the system, and r_1 is the vertical radius of curvature, negative for the usual, concave shaped meniscus [66] (see figure 4.5). In thermal equilibrium this radius is given by the Kelvin equation [60]:

$$r = \frac{\gamma \upsilon_0}{kT \ln p/p_s}, \tag{4.10}$$

where γ is the surface tension, υ_0 is the molecular volume of the liquid, k is the Boltzmann constant, T is the system temperature and p/p_s is the relative humidity.

The shape of the meniscus also defines the xy-projection of the area of the particle to which the negative Laplace pressure Δp focuses. For an area projection of A_{xy} with the Laplace pressure defined as [67]

$$\Delta p = \gamma\left(\frac{1}{r_1} + \frac{1}{r_2}\right) = \frac{kT \ln p/p_s}{\upsilon_0} \tag{4.11}$$

the capillary pressure force (F_{cp}) is given by

$$F_{cp} = A_{xy}\frac{kT\ln p/p_s}{\upsilon_0} \tag{4.12}$$

and the surface tension force (F_{st}) by

$$F_{st} = l \cdot \gamma\cos\alpha, \tag{4.13}$$

where l is the perimeter of the contact between the meniscus and the particle and $\gamma\cos\alpha$ is the vertical component of the surface tension (see Fig. 4.5).

4.3.1 Aspects of adhesion geometry

Very significant parameters, which largely determine the strength of the capillary force, are the contact angles (θ_1 and θ_2 in Fig. 4.5), *i.e.* hydrophilicity or hydrophobicity of the surfaces. As hydrophobicity increases, the projected area A_{xy} decreases leading to a smaller capillary pressure force. Ultimately, the condensation of the liquid cell becomes impossible when the contact angles reach 90° leading to humidity independent adhesion.

The particle shape has a strong effect on the humidity dependence of the capillary force, since the humidity dependence of the area A_{xy} depends strongly on the particle shape. For example, for blunt shapes, the area increases very rapidly when the size of the meniscus increases. Often the experiments are done by assuming a perfect spherical geometry of the particle. This is sensible, as small deviations from the shape do not result in large changes in forces. If one, however, tries to model the capillary force between an SFM tip and a surface by assuming conical or truncated conical tip shapes, much more caution is needed.

The separation between the particle and the surface has a different impact on the humidity dependence as can be seen from Fig. 4.6 where the separation H is varied for a spherical particle. The increasing separation induces a lower limit of humidity, below which a meniscus is not formed, and also changes the humidity where the maximum force is obtained. The curves tend towards a common value at the highest humidities, because then the meniscus is over 10 nm in height, and small changes (of a few ångströms) in particle–surface separation do not have a large effect.

4.3.2 Experiments and comparison to theory

The humidity dependence of adhesion was also studied experimentally using several particle sizes and shapes and the results were compared to the theory. The

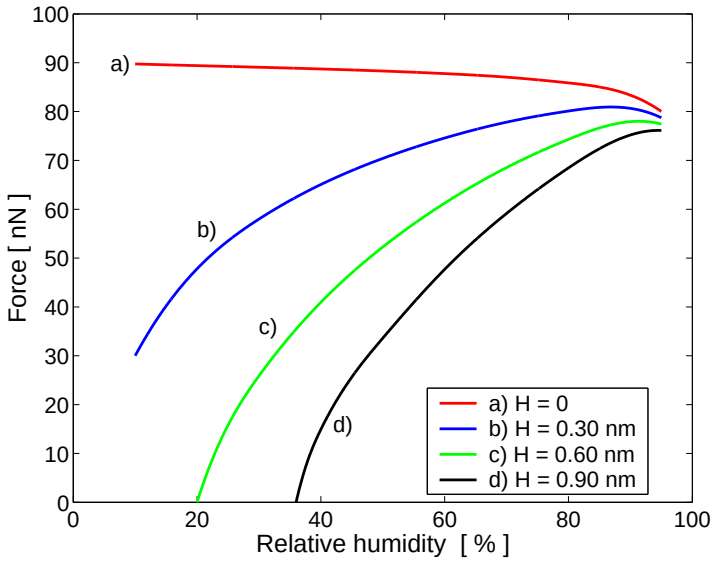

Figure 4.6: The effect of particle–surface separation on the humidity dependence of the capillary force for a spherical particle, $R = 100$ nm.

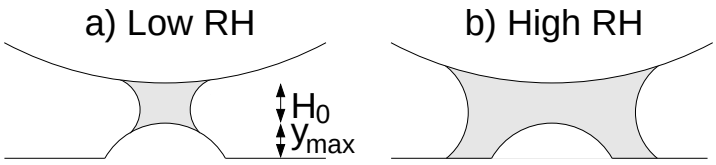

Figure 4.7: Model for advancing meniscus formation on surfaces with finite roughness [53], a) with low humidities the meniscus is formed between the particle and the asperity on the surface, b) with increased humidity the meniscus extends over the asperity filling the volume between the particle and the substrate.

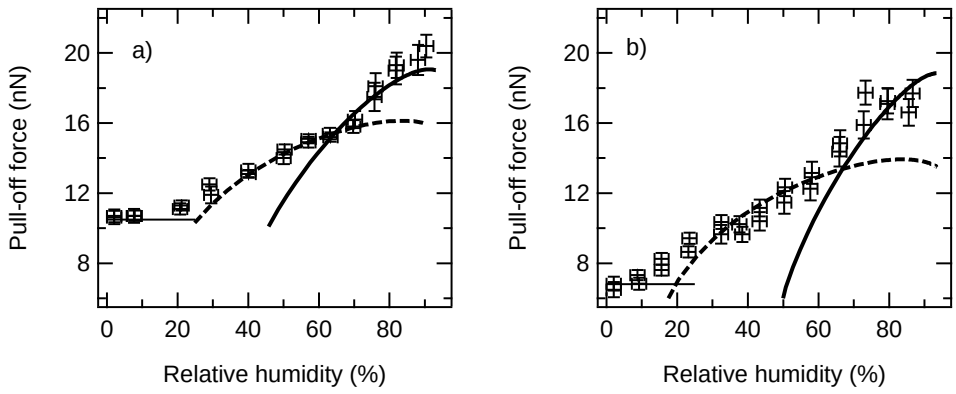

Figure 4.8: Pull-off forces for small silica particles on a) SiO_2 and b) TiO_2 surface as a function of humidity. The dashed and solid lines represent theoretical humidity dependence with small and large water meniscus shown in Fig. 4.7.

experiments revealed that in real conditions also the surface roughness has to be taken into account. A model by Ata *et al.* [53] for capillary formation on rough surfaces was used. The model predicts that in low humidities the water meniscus appears between the particle and an asperity on the surface and in higher humidities the film extends to the planar surface below the asperity, as shown in Fig. 4.7.

Fig. 4.8 presents the measured pull-off forces for small silica particles on silica and titania surfaces as a function of humidity. The measured series consist of three regions; humidity independent part below RH 20%, and two humidity dependent parts of advancing meniscus formation as shown in Fig. 4.7. The solid and dashed lines present theoretical behavior assuming spherical line profile of the particles.

The model for the humidity dependence of the adhesion fits to the experimental data well. The shapes of the force–humidity curves are nicely explained by the growth of the water meniscus between the particle and the surface as shown in Fig. 4.7. Since the actual sizes of the particles were not known, the radii of the particles were fitted. The resulting values were reasonable, from 35 to 40 nm, for SFM probes. The shape of the small probes is not exactly known, and can significantly differ from spherical. However, the assumed spherical shape gives reasonable results. The two humidity regions were also present in the studies by Ata *et al.* [53]. However, they did not observe humidity dependence inside these regions, only a difference in the pull-off force between the two regions. This might result from the unmatched sizes of the particles and the asperities.

The humidity dependence of the adhesion of silica microspheres on silica surface is shown in Fig. 4.9. Experimental data shows for both 1.0 μm and 2.5 μm spheres

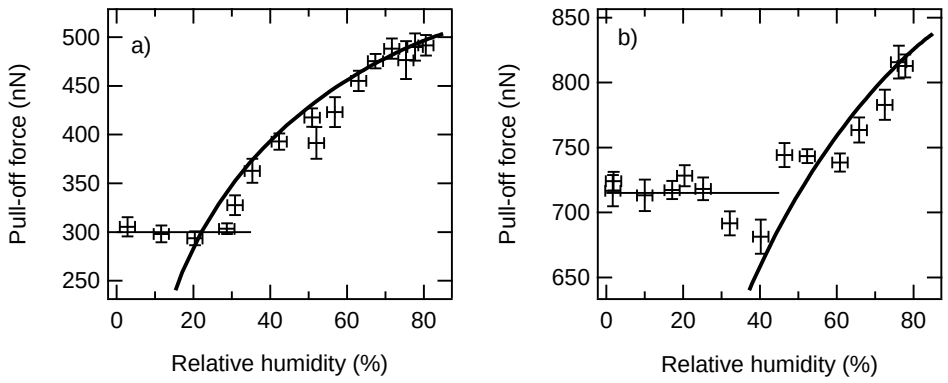

Figure 4.9: Pull-off forces for silica microspheres on silica surface as a function of humidity, a) R=1.0 μm and b) R=2.5 μm.

two regions; at low humidities the adhesion is constant and above RH 30% it starts to increase. The solid lines in Fig. 4.9 represent the theoretical humidity dependence on a flat substrate. The best fit radii for the 1.0 μm and 2.5 μm spheres were 0.75 μm and 1.2 μm, respectively. The calculated force–humidity curves seem to reproduce the measured data if the radii of curvatures are assumed smaller than the radii determined from the scanning electron microscope (SEM) images. This can be interpreted as the part of the spheres making the contact with the surface having some corrugation giving rise to a smaller local radii than those of the whole spheres. There is, however, only one humidity dependent region, because the particles are much larger than the surface asperities. The relative increase in the adhesion due to humidity decreases with an increasing particle size.

In order to compare experiments with other particle shapes than spheres to the theory, some SFM probes were modified by eroding them against a rough surface. The assumed blunt shape was confirmed by SEM measurements together with reverse AFM imaging. Fig. 4.10 presents the humidity dependence measured for these probes. The curves have clear concave shape compared to convex shape for the spherical particles. The theoretical curves in Fig. 4.10 are calculated using truncated cones by fitting the size of the flat part as well as the half cone angle resulting in good agreement with the experiments. However the fitted parameters differed significantly from the expected values. Apparently the probes have apex with small flat part and large half cone angle.

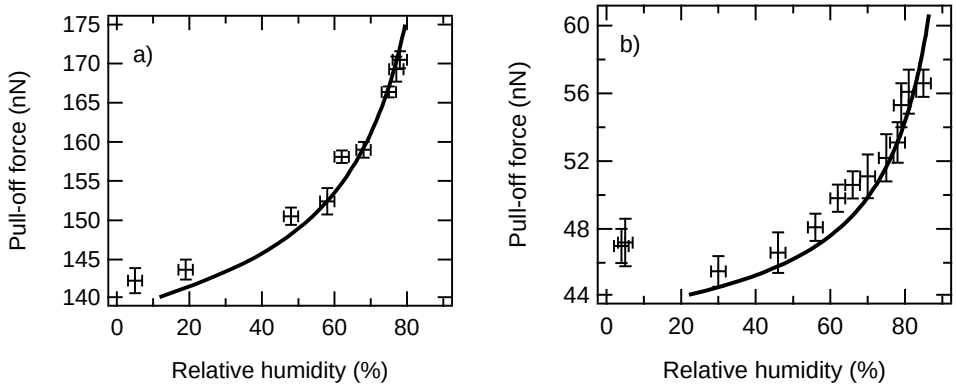

Figure 4.10: Pull-off forces for blunt silica particles on silica surface as a function of humidity, a) smaller and b) larger blunt particle.

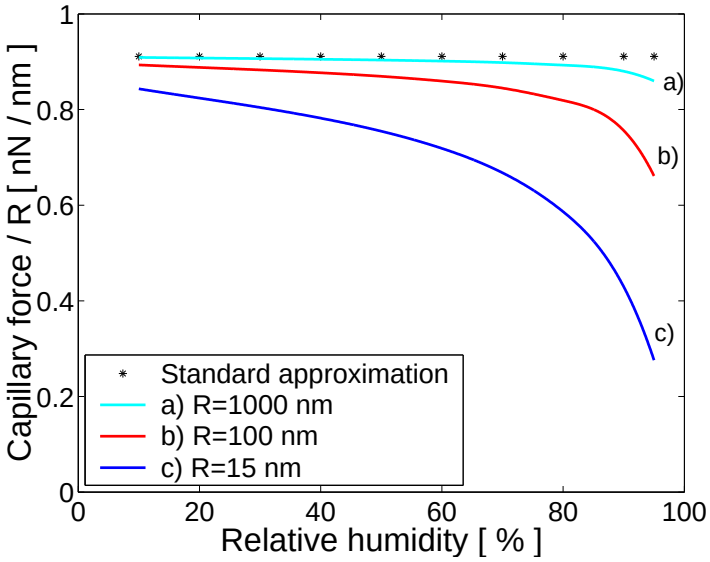

Figure 4.11: Applicability of the standard model of capillary force for different particle sizes, showing the humidity dependence of the capillary pressure force for spherical particles with zero particle–surface separation (H_0).

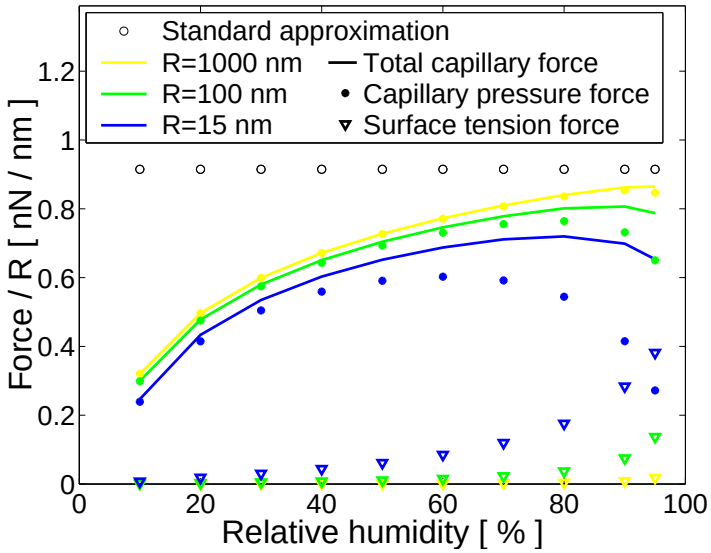

Figure 4.12: Humidity dependence of the capillary force components at 3 Å particle–surface separation.

4.3.3 Validity of some generally used approximations

With the exact model for capillary forces, the validity of generally used approximations may be evaluated. One of the most common approximations applied is the *standard approximation* [58, 60, 68] for the capillary force:

$$F_c = 4\pi\gamma R\cos\theta, \tag{4.14}$$

which is in fact humidity independent. This approximation is derived for micron sized sphere on a flat surface assuming equal contact angles and no surface tension component. The calculations for the capillary pressure force show (see figure 4.11), that the standard approximation really is valid for spheres larger than 1 μm radius, but below that a strong humidity dependence arises. This is particularly important in SFM experiments, as tips usually have a radius in the range of 10–100 nm. The applicability of the standard model even for large particles is, however, very limited since it is derived for vanishing separation between the particle and the surface. With finite separation there is a humidity dependence shown in fig. 4.12, although weak for large particles. This dependence is also seen experimentally in Fig. 4.9 where neither of the particles satisfy humidity independence.

It is also often assumed [60] that the surface tension force is negligible compared to the capillary pressure force for all but the highest humidities. However, the

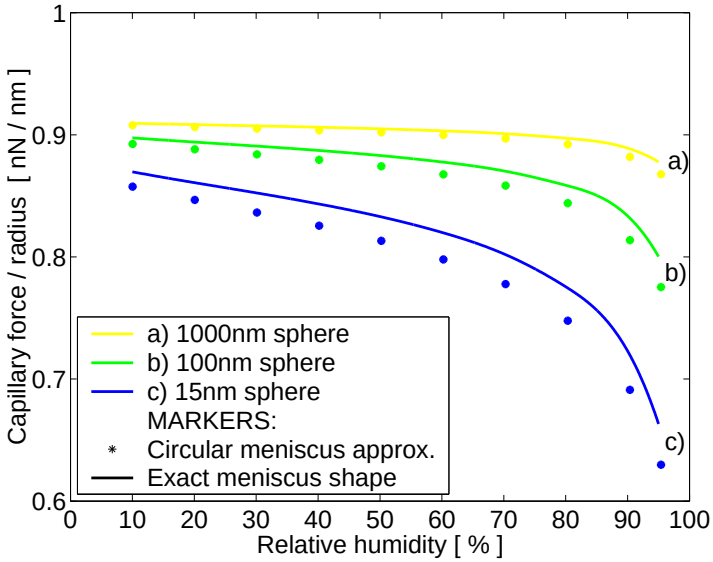

Figure 4.13: Capillary forces calculated with circular profile approximation, compared to exact profile. For a 1000 nm radius sphere the match is more or less perfect, for a 100 nm sphere there is an error of about 1 %, and for a 15 nm sphere the error is about 2–3 %.

results in Fig. 4.12 show that this also strongly depends on the particle size. The surface tension force is negligible with 1 μm radius spherical particles, but for particles with a 15 nm radius it can be larger than the capillary pressure force. Generally it is assumed that the capillary force can be calculated by using a circular meniscus profile. The results, shown in figure 4.13, for spheres of different radii, show that this approximation is justified in the size range where continuum modeling can be used.

Chapter 5

Summary

In this work bonding to surfaces has been studied using surface sensitive methods. Adsorption of benzene on low index cobalt surface has been studied in ultra high vacuum conditions using electron spectroscopies. The detailed adsorption structure of benzene has been determined by low energy electron diffraction. Adhesion of nano- and micrometer sized particles has been studied by force measurements carried out using a scanning force microscope. The impacts of surface roughness and ambient humidity on adhesion have been discussed.

Two different adsorption structures for benzene on the Co(0001) surface were demonstrated. The structure was determined by the adsorption temperature and exposure. The nominal coverages of the structures were 1/8 and 1/7. Adsorbed benzene was found to partly dehydrogenate during heating, leaving C_6H_5 fragments on the surface. The activation energy for the dehydrogenation was determined to be 102 kJ/mol.

In the detailed analysis, a benzene molecule was found to adsorb on an hcp site, the two parallel C–C bonds aligned in $[1\bar{1}00]$ direction. The distance between the molecule and the first substrate layer was expanded slightly from the value calculated from the radii of the atoms, indicating relatively weak bonding. The carbon–carbon bond lengths stayed in their gas phase value. The C–H bonds were slightly expanded and bent away from the substrate. The benzene induced significant buckling in the first substrate layers, although LEED and DFT studies did not fully agree on the magnitude of the buckling. DFT calculations also left the adsorption site open with two equally preferable sites.

In adhesion studies of nano- and micrometer sized particles it has been shown that the relative size of the particle and the surface features is of fundamental importance. Adhesion on rough surfaces was divided into two regions depending if the particle is smaller or larger than the typical asperity on the surface. For small

particles the adhesion was determined by a single contact with the surface alone, whereas large particles had several contacts with the surface due to asperities under it. The key parameters, which determined the strength of the adhesion, were the curvature and the density of the asperities and the size of the particle.

Capillary bridge formation due to ambient humidity was found to have a significant effect on the adhesion for nanometer sized hydrophilic particles. For particles well above 1 μm radius the adhesion was humidity independent. The particle shape had a strong effect on the strength of the humidity dependence whereas the separation between the particle and the surfaces determined the lowest limit for capillary formation, observed in both experiment and theory. Adhesion measurements showed an advancing capillary bridge formation on surfaces with nanoscale roughness leading to two separate capillary regions. Initially the capillary bridge was formed between the particle and the asperities on the surface further advancing to cover also the volume between the particle and the substrate as the humidity increases. The validities of some generally used approximations were also discussed.

Bibliography

[1] C. J. Davisson and L. H. Germer, Phys. Rev. **30**, 705 (1927).

[2] J. B. Pendry, *Low Energy Electron Diffraction; The Theory and Its Application to the Determination of Surface Structure* (Academic Press, London, New york, 1974).

[3] M. A. van Hove, *Surface crystallography by LEED: theory, computation and structural results* (Springer, Berlin, Heidelberg, 1971).

[4] J. B. Pendry, J. Phys. C: Solid State Phys. **13**, 937 (1980).

[5] G. Binnig, H. Rohrer, C. Gerber, and E. Weibel, Phys. Rev. Lett. **49**, 57 (1982).

[6] G. Binnig, C. Quate, and C. Gerber, Phys. Rev. Lett. **56**, 930 (1986).

[7] T. R. Albrecht, P. Grütter, D. Horne, and D. Rugar, J. Appl. Phys. **69**, 668 (1991).

[8] *Noncontact Atomic Force Microscopy*, edited by S. Morita, R. Wiesendanger, and E. Mayer (Springer, Berlin, Heidelberg, 2002).

[9] Q. Zhong, D. Inniss, K. Kjoller, and V. B. Elings, Surf. Sci. Lett. **290**, L688 (1993).

[10] B. Cappella and G. Dietler, Surf. Sci. Rep. **34**, 1 (1999).

[11] H.-J. Butt, B. Cappella, and M. Kappl, Surf. Sci. Rep. **59**, 1 (2005).

[12] G. Attard and C. Barnes, *Surfaces* (Oxford University Press, New York, 1998).

[13] *Practical surface analysis*, 2nd ed., edited by D. Briggs and M. P. Seah (Wiley, Chichester, 1990), Vol. 1.

[14] P. Jacob and D. Menzel, Surf. Sci. **201**, 503 (1988).

[15] W. Huber, H.-P. Steinrück, T. Pache, and D. Menzel, Surf. Sci. **217**, 103 (1989).

[16] A. Wander *et al.*, Surf. Sci. **249**, 21 (1991).

[17] W. Huber, P. Zebisch, T. Bornemann, and H.-P. Steinruck, Surf. Sci. **258**, 16 (1991).

[18] C. Stellwag, G. Held, and D. Menzel, Surf. Sci. **325**, L379 (1995).

[19] O. Schaff *et al.*, Surf. Sci. **248**, 89 (1996).

[20] W. Braun *et al.*, Surf. Sci. **475**, 18 (2001).

[21] K. M. E. Habermehl-Cwirzen, K. Kauraala, and J. Lahtinen, Physica Scripta **T108**, 28 (2004).

[22] H. H. Graen *et al.*, Surf. Sci. **223**, 33 (1989).

[23] K. Pussi, M. Lindroos, and C. Barnes, Chem. Phys. Lett. **341**, 7 (2001).

[24] C. J. Barnes, M. Valden, and M. Pessa, Surf. Rev. Lett. **7**, 67 (2000).

[25] M. A. van Hove *et al.*, Surf. Sci. Rep. **19**, 191 (1993).

[26] J. P. Perdew *et al.*, Phys. Rev. B **46**, 6671 (1992).

[27] *CRC Hanbook of Chemistry and Physics*, 86th ed., edited by D. R. Lide (CRC Press, Boca Raton, 2005).

[28] G. Held, M. Bessent, S. Titmuss, and D. A. King, J. Chem. Phys. **105**, 11305 (1996).

[29] F. Mittendorfer and J. Hafner, Surf. Sci. **472**, 133 (2001).

[30] S. Yamagishi, S. J. Jenkins, and D. A. King, J. Chem. Phys. **114**, 5765 (2001).

[31] C. Morin, D. Simon, and P. Sautet, J. Phys. Chem. B **107**, 2995 (2003).

[32] T. Vaara, J. Vaari, and J. Lahtinen, Surf. Sci. **395**, 88 (1998).

[33] H. Krupp, Adv. Colloid Interface Sci. **1**, 111 (1967).

[34] D. Tabor, J. Colloid Interface Sci. **58**, 2 (1977).

[35] B. J. Briscoe and S. S. Panesar, J. Phys. D: Appl. Phys. **25**, A20 (1992).

[36] H. Rumpf, *Particle Technology* (Chapman & Hall, London/New York, 1990).

[37] Y. I. Rabinovich *et al.*, J. Colloid Interface Sci. **232**, 10 (2000).

[38] Y. I. Rabinovich *et al.*, J. Colloid Interface Sci. **232**, 17 (2000).

[39] K. Cooper, N. Ohler, A. Gupta, and S. Beaudoin, J. Colloid Interface Sci. **222**, 63 (2000).

[40] K. Cooper, A. Gupta, and S. Beaudoin, J. Colloid Interface Sci. **234**, 284 (2001).

[41] M. Götzinger and W. Peukert, Vacuum **20**, 5298 (2004).

[42] S. Eichenlaub, A. Gelb, and S. Beaudoin, J. Colloid Interface Sci. **280**, 289 (2004).

[43] E. R. Beach, G. W. Tormoen, J. Drelich, and R. Han, J. Colloid Interface Sci. **247**, 84 (2002).

[44] G. W. Tormoen, J. Drelich, and J. Nalaskowski, J. Adhesion Sci. Technol. **19**, 215 (2005).

[45] X. Xiao and L. Qian, Langmuir **16**, 8153 (2000).

[46] L. Zitzler, S. Herminghaus, and F. Mugele, Phys. Rev. B **66**, 155436 (2002).

[47] L. Xu *et al.*, J. Phys. Chem. B **102**, 450 (1998).

[48] D. L. Sedin and K. L. Rowlen, Anal. Chem. **72**, 2183 (2000).

[49] M. He *et al.*, J. Chem. Phys. **114**, 1355 (2001).

[50] T. Eastman and D. M. Zhu, Langmuir **12**, 2859 (1996).

[51] R. Jones, H. M. Pollock, J. A. S. Cleaverand, and C. D. Hodges, Langmuir **18**, 8045 (2002).

[52] Y. I. Rabinovich *et al.*, Adv. Colloid Interface Sci. **96**, 213 (2002).

[53] A. Ata, Y. I. Rabinovich, and R. K. Singh, J. Adhesion Sci. Technol. **16**, 337 (2002).

[54] C. Gao, P. Dai, A. Homola, and J. Weiss, J. Tribology **120**, 358 (1998).

[55] C. Gao, Appl. Phys. Lett. **71**, 1801 (1997).

[56] A. Marmur, Langmuir **9**, 1922 (1993).

[57] A. de Lazzer, M. Dreyer, and H. Rath, Langmuir **15**, 4551 (1999).

[58] F. M. Orr, L. E. Scriven, and A. P. Rivas, J. Fluid Mech. **67**, 723 (1975).

[59] T. Stifter, O. Marti, and B. Bhushan, Phys. Rev. B **62**, 13667 (200).

[60] J. Israelachvili, *Intermolecular & Surface Forces*, 2nd ed. (Academic Press, London, 1992).

[61] T. Halicioglu and G. M. Pound, Phys. Status Solidi (a) **30**, 619 (1975).

[62] K. L. Johnson, K. Kendall, and A. D. Roberts, Proc. R. Soc. Lond. A. **324**, 301 (1971).

[63] B. Derjaguin, V. Müller, and Y. Toporov, J. Colloid Interface Sci. **73**, 314 (1975).

[64] D. Maugis, J. Colloid Interface Sci. **150**, 243 (1992).

[65] R. H. French, R. M. Cannon, L. K. DeNoyer, and Y.-M. Chiang, Sol. St. Ionics **75**, 13 (1995).

[66] A. W. Adamson, *Physical Chemistry of Surfaces*, 3rd ed. (Wiley, New York, 1976).

[67] F. M. White, *Viscous fluid flow*, 2nd ed. (McGraw-Hill, New York, 1991).

[68] J. S. McFarlane and D. Tabor, Proc. R. Soc. Lond. Ser. A **202**, 224 (1950).